3D RECONSTRUCTION OF SMALL SOLAR SYSTEM BODIES USING PHOTOCLINOMETRY BY DEFORMATION

CAPANNA Claire [1,2], JORDA Laurent [1], LAMY Philippe [1]
(1) Aix-Marseille Université, CNRS, UMR 7326, Laboratoire d'Astrophysique de Marseille, Marseille, France

GESQUIERE Gilles [2]
(2) Aix-Marseille Université, CNRS, UMR 7296, Laboratoire des Sciences de l'Information et des Systèmes, Marseille, France

ABSTRACT

This article tackles the problem of reconstructing the 3D shape model of asteroids and cometary nuclei from images obtained with a visible imaging system aboard a planetary spacecraft. We describe a photoclinometry method based on the optimization of the chi-square difference between observed and synthetic images of the object by deformations of its initial shape, described here as a mesh of triangular facets. The non-linear optimization is performed using the so-called "limited-memory Broyden-Fletcher-Golbfarb-Shanno" algorithm. The deformations can be applied: (i) by modifying the coefficients of a spherical harmonics expansion in order to extract the global shape of the object, and/or (ii) by moving the height of the vertices of a triangular mesh in order to increase the accuracy of the global shape model and/or to derive local topographic maps of the surface. This method has been tested on images of the asteroids Steins and Lutetia obtained by the imaging system aboard the Rosetta spacecraft of the European Space Agency.

KEYWORDS

3D reconstruction, optimization, deformation, spherical harmonics, synthetic images, photoclinometry

1. INTRODUCTION

There are several ways to reconstruct a three-dimensional surface from a set of images. The stereo technique allows to build a network of control points from remarkable features identified at the surface of the object [9]. Stereophotogrammetry, an extension of the former, is a powerful technique widely used to reconstruct digital terrain models of the surface of

planets [3], asteroids [7] or cometary nuclei [6]. More recently, stereophotoclinometry using several images of the same area of the surface under different viewing and/or illumination conditions has been successfully applied to several bodies of our solar system, among them asteroid Itokawa observed by the Hayabusa spacecraft [2].

These three methods require resolved images in which the object is at least ~100 pixels across. Besides, the reconstructed areas need to be imaged with different viewing geometry in order to obtain stereo control points.

We present here a new photoclinometry method in which we apply deformations to a triangular mesh in a non-linear optimization loop until the synthetic images generated from the mesh best-match the observed ones. The deformation can be obtained by modifying the coefficients of a spherical harmonics expansion or by moving the height of the vertices of the triangular mesh above the surface. The first deformation with the spherical harmonics allows the retrieval of the low frequencies of the shape model, whereas the second deformation, based on displacements of vertices, allows to increase the accuracy of the shape model.

The article is organized as follows: we present our method in Section 2, its application to asteroids Steins and Lutetia in section 3 and we finally conclude in Section 4.

2. 3D RECONSTRUCTION METHOD

Our 3D reconstruction method needs an input model described as a mesh of triangular facets. This model can be a sphere or a more refined model obtained with another reconstruction technique.

2.1 Generation of Synthetic Images

Synthetic images are generated using a tool called OASIS (Optimized Astrophysical Simulator for Imaging Systems) [5]. OASIS calculates the position and the orientation of the object in the camera frame. It identifies the facets present in the field of view of each pixel. It then performs ray-casting *(i)* to calculates the projected shadows which implies, for all facets in the field of view in a pixel, a search for occlusions between facets, and *(ii)* to determine which facets of the shape model are illuminated and in view of the camera. For each such facet *i* and each image *n*, it calculates the bi-directional reflectance (BDR) $r_i^{(n)}$ following Hapke's model [4]. The intersected solid angle $\Omega_i^{(p,q,n)}$ between this facet and the pixel *(p, q)* is calculated. The signal $D_{pq}^{(n)}$ received by each pixel (in Digital Number, DN) is then obtained by summing the contributions of all facets in the field-of-view of this pixel:

$$D_{pq}^{(n)} \approx \frac{g \; S_{coll} \; t_e^{(n)}}{h \; c \; (R_h^{(n)})^2} \left(\sum_{i=1}^{M_{pq}} r_i^{(n)} \; \Omega_i^{(pq,n)} \rho_i \right) \tag{1}$$

where *g* is the gain of the electronics, S_{coll} is the collecting surface of the telescope, $t_e^{(n)}$ is the exposure time of the image number *n*, $R_h^{(n)}$ is the heliocentric distance of the object (in astronomical units), *h* is Planck's constant, *c* is the light speed, ρ_i is a pre-calculated absolute

calibration factor. Finally, the image is convolved with the point-spread-function of the instrument.

2.2 Deformations of the Shape Model

2.2.1 Deformation based on Spherical Harmonics

Spherical parameterization of a triangular mesh shape model has been developed in the last three decades. Spherical harmonics $\{\Upsilon_{lm}(\phi,\varphi): m \in \mathbb{Z}, |m| \leq l \in \mathbb{N}\}$ are orthogonal functions defined on the unit sphere $\mathbb{S}^2$:

$$\Upsilon_{lm}(\theta,\varphi) = (-1)^m k_{lm} \, \mathrm{P}_{lm}(\cos\theta) \, \mathrm{e}^{im\varphi} \tag{2}$$

where k_{lm} is a constant and P_{lm} is the associated Legendre polynomial such as:

$$\mathrm{P}_{lm}(x) = \frac{(-1)^m}{2^l \, l!} \sqrt{(1-x^2)^m} \, \frac{d^{l+m}}{dx^{l+m}} (x^2 - 1)^l \tag{3}$$

The spherical harmonics transform [11] is used to decompose the input model in the frequency domain. The coordinates $\mathbf{R'}_k$ of the vertices are described as:

$$\mathbf{R}_k^{'} = \mathrm{R}_k \cdot \begin{pmatrix} \sin\theta_k \cos\varphi_k \\ \sin\theta_k \sin\varphi_k \\ \cos\theta_k \end{pmatrix} \tag{4}$$

where the coordinates (θ_k, φ_k) define the vertices of a pre-defined triangular mesh in a spherical coordinates system and R_k is a spherical function ($\mathrm{R}_k : \mathbb{S}^2 \to \mathbb{R}$) given by the following linear combination:

$$\mathbf{R}_k = \sum_{l=0}^{l_{max}} \sum_{m=-l}^{+l} C_{lm} \; \mathrm{Y}_{lm}(\theta_k, \varphi_k) \tag{5}$$

where $\mathrm{Y}_{lm}(\theta, \varphi)$ are the real form of the spherical harmonics functions $\mathbf{Y}_{lm}$. In this representation, the parameters C_{lm} define the shape of the object. The number of coefficients depends on the degree l_{max} of the above expansion. Increasing its value allows us to reach higher frequencies in the 3D representation of the object. In the following we will call "SHO" the spherical harmonics optimization and "SHO model" the final model resulting from this optimization.

2.2.2 Deformation based on Vertex Offsets

In order to increase the accuracy of the spherical harmonics model or of the input model, we introduce another deformation scheme in which we directly modify the height of the vertices with respect to the initial mesh used as starting points in the optimization process. We calculate the vector $\mathbf{N}_k$ normal to the surface at the vertex k by averaging the normal vectors $\mathbf{N}_i$ of the V_k facets which share this vertex:

$$\mathbf{N}_k = \frac{\sum_{i=1}^{V_k} S_i \, \mathbf{N}_i}{\sum_{i=1}^{V_k} S_i} \tag{6}$$

where S_i is the surface of the facet number i .

The modification of the height H_k of the vertex k is applied in the direction $\mathbf{N}_k$. The coordinates $\mathbf{R'}_k$ of the vertex after this deformation become:

$$\mathbf{R}_k^{'} = \mathbf{R}_k + H_k \, \mathbf{N}_k \tag{7}$$

The coefficients H_k are initially set to zero and their value is modified during the optimization. In the following we will call "VHO" the vertices height optimization and "VHO model" the final model resulting from this optimization.

2.3 Optimization of the Parameters

2.3.1 Shape Model

We want to minimize the reduced chi-square between the pixel values $F_{pq}^{(n)}$ of the N observed images and those of the corresponding synthetic images given by Eq. (1):

$$\chi^2(P_k) = \frac{1}{N_p} \sum_{n=1}^{N} \sum_{pq} \frac{\left(F_{pq}^{(n)} - \mathrm{D}_{pq}^{(n)}(P_k)\right)^2}{\left(\sigma_{pq}^{(n)}\right)^2} \tag{8}$$

where N_p is the total number of pixel and $\sigma_{pq}^{(n)}$, the uncertainty on the observed pixel value, is given by:

$$\sigma_{pq}^{(n)} = g \sqrt{\frac{D_{pq}^{(n)} t_e}{g} + \sigma_R^2} \tag{9}$$

where σ_R is the readout noise. In Eq. (8), the free parameters (variables) P_k are the coefficients C_{lm} for SHO (section 2.2.1) and the heights H_k for VHO (section 2.2.2).

For SHO, the spherical harmonics coefficients C_{lm} are optimized following a multi-resolution scheme. The variable l_{max}, which determines the number of optimized parameters, is progressively increased. For low values of l_{max}, only low spatial frequencies of the shape model are constrained. Increasing the value of l_{max} leads to retrieve higher spatial frequencies.

In order to minimize the chi-square function (8), we use a non-linear optimization algorithm called "limited memory Broyden-Fletcher-Golbfarb-Shanno" (L-BFGS), a quasi-Newton optimization method [1]. It is well suited for large scale optimization problems and it requires a limited amount of memory. A typical number of 50 to 100 iterations of the algorithm is required before it converges to a stable value P_k of the free parameters. At the end of the optimization, the coordinates $\mathbf{R'}_k$ of the vertices define the final shape model.

The L-BFGS method requires the calculation of the partial derivatives at each iteration. These derivatives are calculated with the finite difference method, in which two chi-square values need to be calculated for each partial derivative using Eq. (8):

$$\frac{\partial \chi^2}{\partial H_l}(H_k) = \frac{\chi^2(H_{k'}, H_l + \varepsilon_H) - \chi^2(H_{k'}, H_l - \varepsilon_H)}{2\ \varepsilon_H} \tag{10}$$

where the index $k' = 1, ..., l–1, l+1, ..., N_v$, with N_v defined as the total number of vertices.

2.3.2 Local Error Calculation

For each pixel (p, q) of image number n, we calculate the residual value in units of the instrumental noise at the end of the optimization using the notation of section 2.3.1:

$$\mu_{pq}^{(n)} = \frac{F_{pq}^{(n)} - D_{pq}^{(n)}(P_k)}{\sigma_{pq}^{(n)}} \tag{11}$$

We "transfer" the value of the residuals from the pixels to the facets using the pixel–facets intersection solid angles $\Omega_i^{(p,q,n)}$ calculated earlier in section 2.1:

$$\mu_i = \frac{1}{N_p\ \Omega_P} \sum_{n=1}^{N} \sum_{pq} \Omega_i^{(pq,n)} \mu_{pq}^{(n)} \tag{12}$$

where Ω_P is the total pixel solid angle, and the second sum runs over the pixels (p, q) intersecting the facet number i. We then calculate the effect of a variation of the slope of each facet on the measured signal, normalized to its associated instrumental noise. The derivative $dD_i/d\varepsilon$ (in DN/°) of the signal with respect to a change of slope is obtained numerically by calculating the mean variation of the signal $D_i^{(n)}$ from Eq. (1) when the vector normal to each facet remains on a cone of axis $\mathbf{N_i}$ (the normal to the surface of the facet) and of half-cone

aperture ε. The error ξ_i on the slope of each facet is deduced from μ_i , $d\mathrm{D}_i/d\varepsilon$, and from the instrumental noise σ_i associated to the signal D_i (Eq. 8):

$$\xi_i = \frac{|\mu_i| \ \sigma_i}{d\,\mathrm{D}_i/d\varepsilon} \tag{13}$$

We take a typical value of $\varepsilon \sim 1°$ to estimate the value of the derivative $d\mathrm{D}i/d\varepsilon$. Knowing the error on the slope, the error on the heights (parameters H_k) can be deduced. The parameter ξ_i forms what we call the "slope error map".

2.3.3 Additional Parameters

Additional parameters can be optimized in the same way if they have an impact on the synthetic images, for instance:
 − the parameters which describe the BDR of the surface,
 − the three angles describing the pointing direction and roll angle of the camera for each individual image,
 − the three Euler angles describing the orientation of the object in space.
 The accuracy in the reconstruction of these parameters by the space agencies is usually not sufficient to retrieve a shape model or a Digital Terrain Model of the object. Therefore, we always need to perform iterative optimizations of the shape, of the pointing direction and roll angle of the camera.

2.4 Speeding up the Calculation of the Partial Derivatives

Most of the CPU time during the optimization process is used to calculate the partial derivatives of the chi-square function defined by Eq. (10) with respect to each parameter. In the case of VHO, when the number of parameters is equal to the number of vertices N_v, it is possible to drastically reduce it.
 Eq. (10) implies the calculation of two chi-square values, i.e., the calculation of $2N_p$ pixel values. A test of occultation between facets has to be done to evaluate the value of each pixel (cf. section 2.1), which implies that the calculation time is proportional to $N_{V/Px}^2$ where $N_{V/Px}$ is the number of vertices per pixel.
 The total calculation time for an iteration becomes:

$$t_{cal} \propto N_v \ N_p \ N_{V/Px}^2 \tag{14}$$

Whereas N_v cannot be modified, a major gain is possible by restricting N_p to those pixel values which are modified when we move the height of a vertex from H_l to $H_l \pm \varepsilon_H$ (see section 2.4.1). It is then possible to extract the final partial derivative from these values (see section 2.4.2).

2.4.1 Calculation of Updated Pixel Values

The calculation of the pixel values modified by a change of the height of the vertex number l from its original value H_l to $H_l \pm \varepsilon_H$ is performed in the following steps.

i. We identify the facets $F_l^{(n)}$ which share the vertex number l and we identify the nominal set of pixels $S_l^{(n)}$ intersected by these facets. We then determine a new set of pixels $S_{l,\pm}^{(n)}$ intersected by the facets after modifying the height of the vertex number l. The set of pixels potentially modified by a displacement of this vertex is the union: $P_l^{(n)} = S_l^{(n)} \cup S_{l,\pm}^{(n)}$.

ii. We identify the facets $F_l^{(n)}$ which are both illuminated and in view of the observer taking into account the displacement $\pm \varepsilon_H$ of the vertex.

iii. For all these facets, we re-calculate the BDR $r_l^{(n)}$ taking into account the new geometry.

iv. The updated values $D'_{pq}{}^{(n)}(H_k)$ of the pixels $P_l^{(n)}$ are then calculated using the relationship (1).

We repeat this operation for all images ($n = 1..N$). In the following we will call $M_l^{(n)}$ the number of pixels in the set $P_l^{(n)}$.

2.4.2 Calculation of the Partial Derivative of the Chi-Square Function

Let us introduce the contribution of the image number n to the global chi-square of Eq. (8):

$$\gamma^{(n)} = \sum_{pq} \Delta_{pq}^{(n)} \qquad (15) \qquad \text{where:} \qquad \Delta_{pq}^{(n)} : \frac{\left(F_{pq}^{(n)} - D_{pq}^{(n)}(H_k) \right)^2}{\left(\sigma_{pq}^{(n)} \right)^2} \qquad (16)$$

The value of the function $\Delta'_{pq}{}^{(n)}$ corresponding to the updated pixel values $D'_{pq}{}^{(n)}(H_k)$ calculated in section 2.4.2 is calculated in the same way:

$$\Delta_{pq}^{'(n)} = \frac{\left(F_{pq}^{(n)} - D_{pq}^{'(n)}(H_k) \right)^2}{\left(\sigma_{pq}^{(n)} \right)^2} \qquad (17)$$

for $pq \in P_l$. We now call $A^{(n)}$ the set of all pixels of image number n. After modification of the height of a vertex, the pixels which remain unchanged belong to $C_l^{(n)}$. Using these notations, we have $A^{(n)} = C_l^{(n)} \cup P_l^{(n)}$ and the modified chi-square becomes:

$$\chi^{'2} = \frac{1}{N_p} \sum_{n=1}^{N} \left[\sum_{pq \in C_l^{(n)}} \Delta_{pq}^{(n)} + \sum_{pq \in P_l^{(n)}} \Delta_{pq}^{'(n)} \right] \qquad (18)$$

which can be rewritten:

$$\chi^{'2} = \frac{1}{N_p} \sum_{n=1}^{N} \left[\left(\gamma^{(n)} - \sum_{pq \in P_l^{(n)}} \Delta_{pq}^{(n)} \right) + \sum_{pq \in P_l^{(n)}} \Delta_{pq}^{'(n)} \right] \tag{19}$$

This relationship gives us the expression of the chi-square as a function of three parameters. The first parameter, $\gamma^{(n)}$, is calculated once from the nominal image.

The partial derivatives can be calculated with the finite difference of the new chi-square:

$$\frac{\partial \chi^2}{\partial H_l}(H_k) = \frac{\chi^{'2}(H_{k'}, H_l + \varepsilon_H) - \chi^{'2}(H_{k'}, H_l - \varepsilon_H)}{2 \ \varepsilon_H} \tag{20}$$

This calculation is simplified since only the sums of contributions $\Delta_{pq}^{(n)}$ and $\Delta'^{(n)}_{pq}$ have to be calculated:

$$\frac{\partial \chi^2}{\partial H_l}(H_k) = \frac{1}{2 \ N_p \ \varepsilon_H} \sum_{n=1}^{N} \left[\sum_{pq \in P_{l,+}^{(n)}} \left(\Delta_{pq}^{'(n)}(H_{k'}, H_l + \varepsilon_H) - \Delta_{pq}^{(n)}(H_{k'}, H_l + \varepsilon_H) \right) \right.$$

$$\left. - \sum_{pq \in P_{l,-}^{(n)}} \left(\Delta_{pq}^{'(n)}(H_{k'}, H_l - \varepsilon_H) - \Delta_{pq}^{(n)}(H_{k'}, H_l - \varepsilon_H) \right) \right] \tag{21}$$

With this calculation, the CPU time for one parameter is now function of the number of pixels affected by the modifications of its height. The total calculation time for an iteration is now:

$$t'_{cal} \propto N_v \ \left\langle M_l^{(n)} \right\rangle_{l,n} N \ N_{V/Px}^2 \tag{22}$$

where $<M_l^{(n)}>_{l,n} \sim 4$ is the mean number of pixels modified during the calculation of the partial derivative.

The gain in CPU time in the calculation of the partial derivatives between the relationships (10) and (21) is then given by the ratio $t'_{cal} / t_{cal} \sim N_p / (4 \ N)$.

3. APPLICATIONS TO THE ASTEROIDS STEINS AND LUTETIA

3.1 Observations

The Rosetta spacecraft [8] launched in 2004 by the European Space Agency is now on its way to meet its final target, the nucleus of comet 67P/Churyumov-Gerasimenko. During its cruise, Rosetta flew by two asteroids: Steins in September 2008 and Lutetia in July 2010. Images of these two asteroids have been acquired by OSIRIS, the imaging system on board Rosetta. OSIRIS includes a narrow-angle camera (NAC) and a wide-angle camera (WAC) both equipped with the same 2048^2 pixels CCD detector with a pixel field-of-view of respectively 18.8 and 99.6 μrad.

Rosetta flew by Steins at a minimum distance of 802 km; the phase angle[1] varied from 38° to 0° and then increased to almost 140° out-bound. For the following analysis, we use a set of 8 radiometrically and geometrically calibrated images: one image acquired with the NAC from a distance of 5235 km and seven images acquired with the WAC from a distance of 1120 km in-bound (see Fig. 1) to 865 km out-bound. These images correspond to a range of phase angles from 7° to 73°.

Lutetia was flown by at a minimum distance of 3170 km; the phase angle varied from 10° to 0° and then increased to almost 140° out-bound. For the present preliminary tests of shape reconstruction, we use a set of 4 subframes extracted from geometrically calibrated images acquired with the NAC from a distance of 5200 km in-bound (see Fig. 3) to 3670 km out-bound. These images correspond to a range of phase angles from 26° to 110°.

3.2 Steins Reconstruction

3.2.1 Reconstruction Strategy

The shape reconstruction of Steins is performed in two main steps. The first step consists in calculating a low-resolution model with the SHO method. For this, we start from a sphere, for which $C_{00} = R_a = 2.7$ km and the other parameters are set to zero. We use the Hapke parameters [4] describing the BDR derived from a global photometric analysis. We begin optimizing the C_{lm} spherical harmonics coefficients of the shape model with $l_{max} = 2$. We iteratively optimize the shape and the Euler angles describing the pointing of the camera. When a stable solution is reached after 1 iteration, we set the degree of the expansion to $l_{max} = 4$ and we repeat the cycle of shape and Euler angles optimizations until $l_{max} = 20$. The sampling of the shape model is given by a hierarchical triangular mesh [10] of level five built from an icosahedron. The resulting 20480 facets and 10242 vertices ensure that the pixels of the images contain typically a few facets. At the end of this step, we have a SHO model of the asteroid. The corresponding synthetic image is displayed in Fig. 1 (middle panel).

A test was made starting from the same sphere but directly optimizing all the coefficients involved when $l_{max} = 20$. Then the optimization allows to simultaneously obtain low and high

---

[1] The phase angle is the angle between the solar direction and the direction of the observer as seen from the object.

frequencies instead of obtaining the low frequencies first. This results in a grossly erroneous model which corresponds to a local minimum (see Fig. 2).

In a second step, we perform VHO in order to improve the above SHO shape model. We proceed as before by iteratively optimizing the shape model and the Euler angles. After a total of typically 3-5 iterations, the final shape model of the asteroid is obtained (see Fig. 1, right panel). We keep the same sampling of the surface used to derive the spherical harmonics shape model.

The results given in this section were obtained with Eq. (10), which corresponds to the "slow" version of the calculation of the partial derivatives.
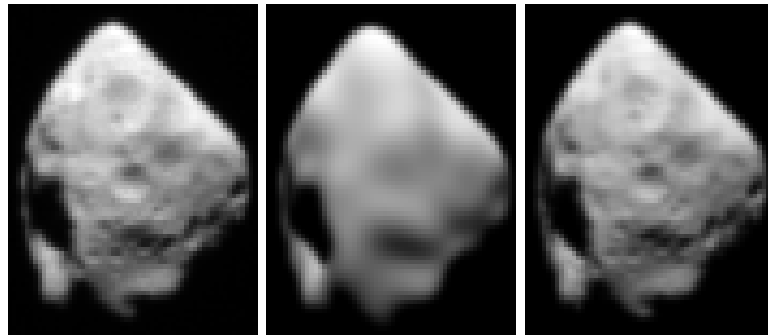
Figure 1. Illustration of the reconstruction methods for one of the eight images of asteroid Steins. Left panel: observed image. Middle panel: synthetic image calculated from the SHO model with the progressive increase of the number of coefficients. Right panel: synthetic image calculated from our final optimized model (VHO).
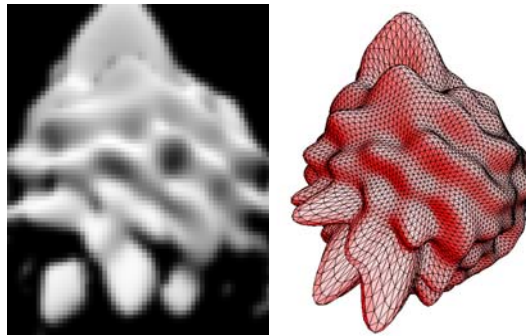

Figure 2. Illustration of an erroneous solution resulting from the reconstruction with spherical harmonics expansion, without a progressive increase of the number of coefficients, for the same image displayed in Fig. 1. The left panel shows the synthetic image calculated from the spherical harmonics model of the right panel.

3.2.2 Final Shape Model

Table 1 summarizes our results. The mean residuals are expressed in units of the instrumental noise. The final mean slope error is calculated from the residuals (section 2.3.2).

The CPU times are given for a dual-core 2 GHz Opteron CPU with 2 GB of RAM. The mean residuals decrease from 9.5 to 6.1 (in units of instrumental noise) from the spherical harmonics to the triangular mesh representation (see also Fig. 1).

Table 1. Summary of our results for SHO and VHO.

Parameters	SHO	VHO
Starting chi-square	28640	90
Final chi-square	90	37
Mean residuals	9.5	6.1
Mean slope error	12°	7°
Mean height error	20 m	10 m
Number of iterations	1	3
Total CPU time	30 hours	3 weeks

3.2.3 Accuracy

As described in Section 2.3.2., residual images can be calculated between synthetic and observed images. Figure 3 shows the residual images of one of the 8 images used to reconstruct Steins after the spherical harmonics expansion optimization (left panel) and after the vertices heights optimization (right panel). On these residual images, a dark grey value corresponds to a higher signal in synthetic images than in the observed ones. The SHO method is unable to reconstruct the small scale topography as illustrated by the absence of craters in the corresponding synthetic image (middle panel of Fig. 1) and conservely their presence in the residual image (left panel of Fig. 3). The VHO method is fortunately able to retrieve all topographic details at all scales as illustrated by the nearly perfect similarity of the observed and synthetic images (respectively left and right panels of Fig.1) and the quasi absence of topographic information in the corresponding residual image (right panel of Fig. 3).

The residual can be projected on the surface (cf. Section 2.3.2.) and Fig. 4 illustrates the results of this projection. Using these maps, we can easily localize the areas where the shape model is not well reconstructed.
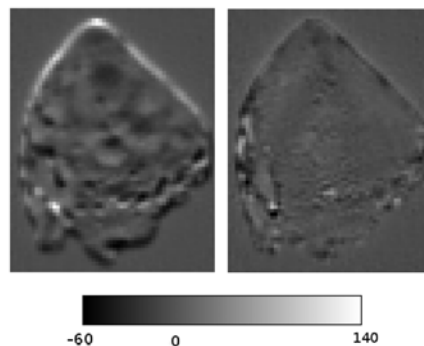

Figure 3. Illustration of a residual image calculated according to Eq. (11), in units of the instrumental noise with SHO (left panel) and our final VHO model (right panel).
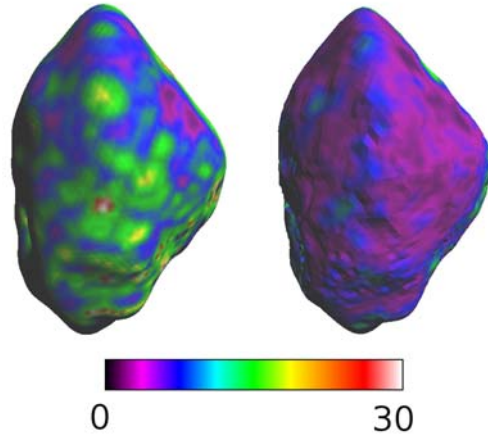
Figure 4. Illustration of the residual images in units of instrumental noise corresponding to Fig. 3 and according to Eq. (12), respectively projected on the SHO model (left panel) and our VHO final model (right panel).

We present in Fig. 5 the histogram of the values in the "slope error map" defined in section 2.3.2 for both the SHO model and our final VHO model. For the latter, the width at half maximum is ~ 7º, which corresponds to 10 m in height, or 1/8th of the pixel resolution at closest approach. The SHO histogram shows a higher value of the mean error.

Larger values of up to ~ 30° are however obtained in regions of the shape model which correspond to the limb[2] and the terminator[3].
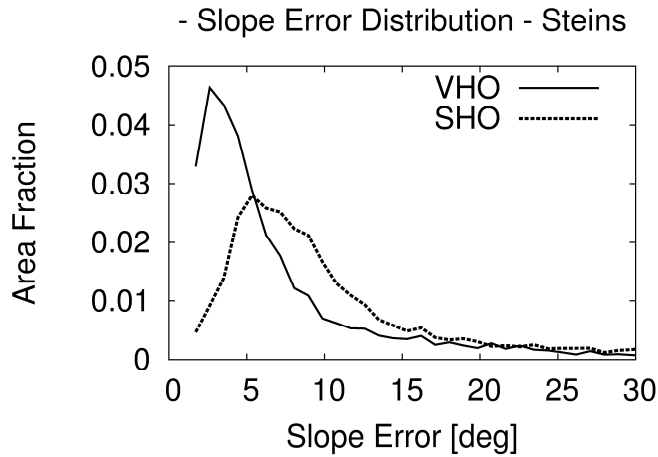

Figure 5. Histograms of the slope error for the models of Steins obtained with VHO (solid line) and SHO (dotted line).

---

[2] The limb is the physical edge of the apparent form of an object.
[3] The terminator is the limit between the illuminated and the dark part of an object.

3.3 Preliminary Tests on Lutetia

Figure 6 shows the result of preliminary tests performed on a 10 km wide Digital Terrain Model (DTM) of the asteroid Lutetia with the VHO method. Our input model is a DTM (also called "maplet") of 10000 facets, extracted from the stereophotoclinometry model (SPC model) of R. Gaskell. Our method allows us to recover higher frequency information (right panel) compared to the initial DTM (middle panel). Craters and grooves (also called "lineaments") are reconstructed with a more accurate depth.
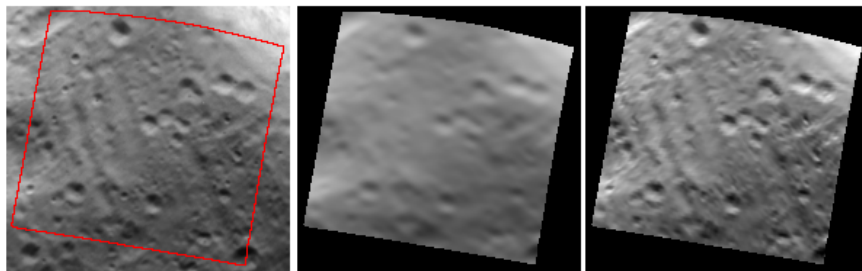

Figure 6. Illustration of the reconstruction method used on asteroid Lutetia. Left panel: observed image. Middle panel: synthetic image calculated from the SPC model. Right panel: synthetic image calculated from our final VHO model.

The comparison between the SPC model and our final VHO shape model is best illustrated in Fig. 7 where the differences in the depths of the different structures can be appreciated.

Figure 7. Perspective views of the DTM shown in Fig. 6.
Left panel: SPC model. Right panel: our VHO model.

We present in Fig. 8 the histogram of the values of the "slope error map" defined in section 2.3.2 for both the SPC shape model and our final VHO model. In the former case, the histogram width at half maximum is ~ 15° whereas it is ~ 10° in the later case which implies a higher accuracy convergence of our optimization method. Note that the absence of limb and terminator on the limited DTM restricts the slope errors to ~ 25° in the VHO histogram. This is not the case of the SPC histogram where error values up to 45° are present. Our new method of photoclinometry by deformation therefore successfully improves the accuracy of the reconstruction compared to the stereophotoclinometry method.
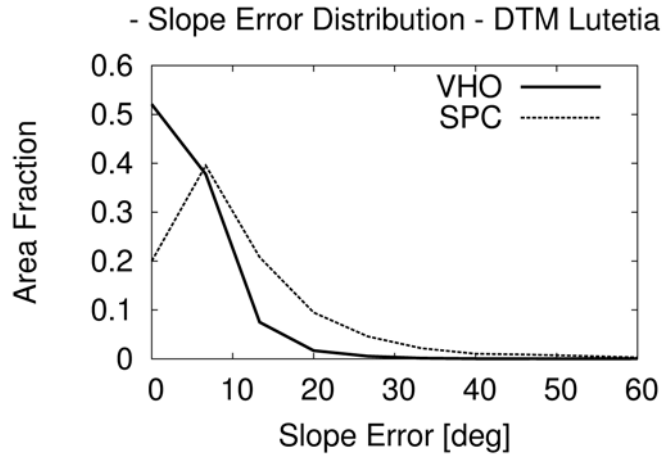
Figure 8. Histogram of the slope error for the models of Lutetia DTM obtained with the VHO and the SPC shape models.

4. CONCLUSION AND FUTURE WORK

We developed and tested a new multi-image photoclinometry method based on deformations applied to a three-dimensional shape model. The method was applied to images of the asteroid Steins acquired by the imaging system on board ESA's Rosetta spacecraft. The method also generates a map of the local topographic error deduced from the pixel residuals, both in slopes and in heights. In the case of Steins, the local averaged slope error amounts to 7°.

Contrary to previous methods mentioned in section 1, our method allows to optimize low-resolution models from images in which the object is less than 100 pixels across.

The "faster" version of the code for the calculation of the partial derivatives of the chi-square described in section 2.4 has been implemented in the code and is in the test and validation process. The first results indicate an overall gain in speed which is in agreement with the prediction of section 2.4.2, i.e., a factor of about 1000 for the example described in section 3. The total CPU time therefore decreases to 30 min.

In the near future, we intend to improve the robustness of the method by implementing a multi-resolution approach also in the VHO deformation scheme. We will also apply this technique to the Lutetia images in order to improve existing high-resolution global shape models [7]. We will also apply it to images of the asteroid Vesta acquired by the framing camera aboard NASA's DAWN spacecraft. Finally, we will use it in 2014 and 2015 to retrieve the shape of the nucleus of comet 67P/Churyumov-Gerasimenko from high-resolution images acquired by the OSIRIS scientific cameras of Rosetta.

REFERENCES

[1] Byrd, R.H. Et al., 1994, Representation of quasi-newton matrices and their use in limited memory methods, *Mathematical Programming* , Vol. 63, No. 4, pp. 129–156, 1994.

[2] Gaskell, R.W. et al., 2008, Characterizing and navigating small bodies with imaging data, *Meteoritics & Planetary science, vol. 43, Issue 6, p. 1049-1061.*

[3] Gwinner, K. et al., 2007, Derivation and validation of high resolution digital terrain models from mars express HRSC-Data, *Photogramm. Eng. Remote Sens.*

[4] Hapke, B., 2002, Bidirectional reflectance spectroscopy 5. The coherent backscatter opposition effect and anisotropic scattering, *Icarus* , vol. 157, pp. 523-534.

[5] Jorda, L. et al., 2010, OASIS: a simulator to prepare and interpret remote imaging of solar system bodies, *Proc. SPIE*, Vol. 7533, No. 753311.

[6] Oberst, J. et al., 2004, The nucleus of Comet Borrelly: a study of morphology and surface brightness, *Icarus,* Vol. 167, pp. 70-79.

[7] Preusker, F. Et al., 2012, The northern hemisphere of asteroid (21) Lutetia -topography and orthoimages from Rosetta OSIRIS NAC image data, Planetary and Space Science, Volume 66, Issue 1, p. 54-63.

[8] Schulz, R., 2009, Rosetta - one comet rendezvous and two asteroid fly-bys, *Solar System Research* , Vol. 43, No. 4, pp. 343-352.

[9] Simonelli, D.P. Et al., 1993., The generation and use of numerical shape models for irregular solar system objects, Icarus , Vol. 103, pp. 49-61.

[10] Szalay, A. et al., 2005*,* Indexing the sphere with the hierarchical triangular mesh, *Tech. Rep. MSR-TR-2005-123, Microsoft Research*

[11] Wiebicke, H.J., 1989, A method for modelling the surface of irregular celestial bodies, *Astron. Nachr.* , Vol. 310, No.2, pp. 159–174.